Plasma Chemistry and Plasma Processing, Vol. 15, No. 4, 1995

Effect of Working Gases on Thermal Plasma Waste Treatment

Seungho Paik,[1] Grant Hawkes,[1] and Hoa D. Nguyen[1]

Received October 3, 1994; revised February 9, 1995

An electric arc melter used for waste treatment processing is numerically studied. The effects of different plasma working gases are studied by using a laboratory scale test reactor. A two-dimensional finite difference approximation is used to solve the set of governing equations. The Navier–Stokes equations coupled with the combined Maxwell's equation for the electromagnetic fields is used to obtain the temperature and flow fields in the arc melter. It is found that the energy efficiency of the air plasma is lower than that of an argon plasma. However, the melted soil volumes are larger using the air plasma than those using the argon plasma. The overall energy efficiency increases as the gap between the cathode and the soil surface decreases. More uniform gas temperatures are found for the air plasma than that for the argon plasma. Result obtained from the laboratory-scale arc melter is used as an input of the energy absorbed into the soil for the USBM arc melter simulation. Results show a maximum temperature of 2195 K at the center of the heat generation and a molten soil exit temperature of 1600 K.

KEY WORDS: Waste destruction; arc melter; plasma gases; analytical.

1. INTRODUCTION

An arc melter is being used for vitrification of thermally oxidized, buried, transuranic (TRU) contaminated wastes by Idaho National Engineering Laboratory (INEL) in conjunction with the U.S. Bureau of Mines (USBM) as a part of the Buried Waste Integrated Demonstration (BWID) project.[1] Even though plasma arc technology has been successfully used for many material processing purposes, there is a lack of information for the application of arc melter technology to the thermal treatment of mixed TRU contaminated wastes and soils. Understanding of those processes requires detailed information on the plasma arc, the molten pool, and geometric configurations. Because of the complex nature of the plasma, experimental work is limited to measuring temperature and the global heat transfer

[1]Idaho National Engineering Laboratory, P.O. Box 1625, Idaho Falls, Idaho 83415-3880.

0272-4324/95/1200-0677$07.50/0

rate rather than obtaining localized information which may be important for determining the optimum operating conditions in the plasma reactor. Instead, numerical modeling of the process has been successfully used for obtaining detailed information.

One of the interesting features of the USBM arc melter is that air is used as a working gas for the plasma. Different working gases have different heating characteristics on the waste as well as on arc melter operating conditions. Usually inert gases, such as argon, helium, etc., are used for the working gas in the dc plasma arc because they yield stable operating environments. Compared to those inert gases, air is difficult to break into a plasma because more heat is required to sustain the plasma state. It is one of the primary purposes of this study to find out the differences between the air and inert gas (in this study, argon was selected since it is one of the most widely used working gases for the dc arc). Heating efficiency and the melt pool shape are compared with different working gases. A laboratory-scale arc melter is modeled to study the various effects of the different working gases.

The plasma arc has been investigated by various researchers.[2-5] Earlier work on this subject was concentrated on modeling the near electrode regions (both anode and cathode) where the major focus of the models was studying the sheath layers formed near the electrodes.[2] Good agreement between spectrometric measurements and the numerical predictions was found. Tsai and Kou[3] studied the cathode-geometry effect on the flow and temperature fields of the welding arcs. They found that the calculated flow and temperature fields were sensitive to the current density distribution along the cathode tip. Pfender[4] discussed the various heat transfer modes in the plasma arc. Recent work of Gonzalez *et al.*[5] focused on studying the metal vapor effects on the heat transfer mechanism during metal scraping using a transferred arc. For the moderate current intensities, they concluded that the presence of the metal vapor significantly affects the radiation heat transfer. Heat conduction in the anode region was considered in their work. The use of arc plasma for refractory metal oxides has been considered by Taniuchi[6]. For this application, the plasma interaction with the processing material was the most important factor in optimizing the design of a processing reactor.

Most of the previous numerical studies on this subject were confined to either the arc plasma region only or the molten material domain only. There is a lack of studies on the combined effects of plasma, molten waste, and the geometric configuration of the confinement. Recently, Paik and Nguyen[7] studied the combined effect of the plasma and the molten waste. Their work focused on the effects of various arc melter operating conditions with a laboratory-scale arc melter using argon as a working gas. In this

study, the combined efforts of simulating the system of the USBM arc melter are undertaken by modeling the full-scale arc melter with the laboratory-scale arc melter model used in Ref. 7. By using the information on the heating efficiency, the full-scale USBM arc melter is modeled with a simplified mathematical model. For the full-scale USBM arc melter simulation, surface-to-surface, gray-body radiation heat transfer is considered along with conduction and advection heat transfer mode. The value of this numerical study will be to aid in understanding the plasma arc-Joule heating process and help design melter geometry and electrode configuration. Further, calculation of the chemical reactions during vitrification of waste based on the flow and temperature fields obtained in this study will help to track chemical composition of off-gas products and finally help compare the designs of different plasma-arc facilities.

In the following, the mathematical model of the laboratory scale arc melter is described in Section 2. The laboratory-scale arc melter model is used for the calculation of energy efficiency (i.e., the percentage of the energy absorbed by the soil to the total energy), and the energy efficiency is used as an input for the USBM melter model described in Section 3. Numerical methods used in this study are described in Section 4 and results are discussed in Section 5. Finally, conclusions based on the obtained results are outlined in Section 6.

2. MATHEMATICAL MODEL OF LABORATORY-SCALE ARC MELTER

This section describes the laboratory-scale arc melter used in this study. Detailed plasma gas modeling and liquid/solid soil interactions are described.

2.1. Geometric Configuration

The geometry for the laboratory-scale arc melter is shown in Fig. 1. The calculation domain is divided into the plasma gas and the soil (either liquid or solid) regions. The dimensions of the soil volume are fixed while the plasma arc length (gap: the distance between the cathode tip and the soil surface) is varied for the calculations. The dimensions of the reactor used in this study resemble the experimental apparatus of Kong *et al.*[8] which has been used to study thermal waste treatment.

2.2. Assumptions

A steady, axisymmetric, and laminar plasma flow is assumed. Local thermodynamic equilibrium (LTE) is assumed in order to simplify mathematical formulations. As a consequence, the plasma is treated as a single

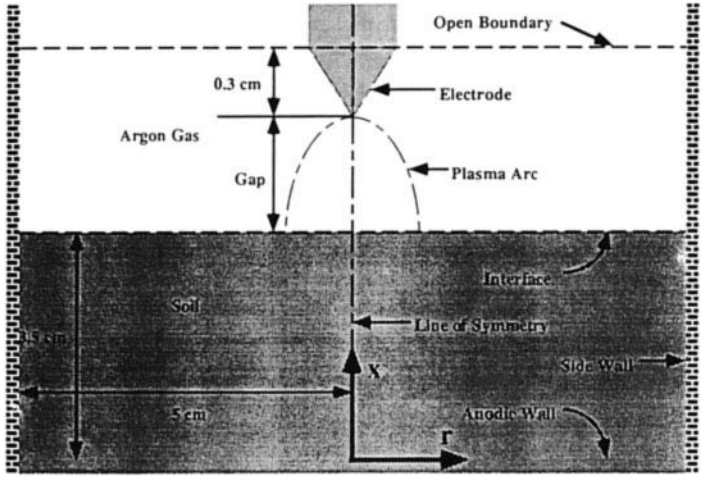

Fig. 1. Geometry of the laboratory-scale plasma arc melter considered in this study.

continuous fluid with only one representative temperature for the flow. The plasma is assumed to be optically thin, which implies that reabsorption of radiation compared with the total radiation energy loss over all wavelengths is insignificant.

2.3. Governing Equations

Based on the above assumptions, the governing equations, without considering erosion effects of the electrodes, may be written in terms of cylindrical coordinates (r, x, θ) as follows:

Conservation of mass

$$\frac{\partial}{\partial x}(\rho u)+\frac{1}{r}\frac{\partial}{\partial r}(\rho r v)=0 \tag{1}$$

where x and r are the axial and radial coordinates, ρ is the density, and u, v are the axial and radial velocity components.

Conservation of momentum

$$\rho u\frac{\partial u}{\partial x}+\rho v\frac{\partial u}{\partial r}=-\frac{\partial p}{\partial x}+j_r B_\theta-\left[\frac{1}{r}\frac{\partial}{\partial r}(r\tau_{rx})+\frac{\partial \tau_{xx}}{\partial x}\right] \tag{2}$$

$$\rho u\frac{\partial v}{\partial x}+\rho v\frac{\partial v}{\partial r}=-\frac{\partial p}{\partial r}-j_x B_\theta-\left[\frac{1}{r}\frac{\partial}{\partial r}(r\tau_{rr})-\frac{\tau_{\theta\theta}}{r}+\frac{\partial \tau_{rx}}{\partial x}\right] \tag{3}$$

where p, j_r, j_x, and B_θ are the pressure, the radial and axial current densities, and the azimuthal self-induced magnetic field component, respectively, and the τ_{rx}, τ_{xx}, τ_{rr}, $\tau_{\theta\theta}$ are the components of the stress tensor which are defined as

$$\tau_{rr} = -2\mu \frac{\partial v}{\partial r}, \qquad \tau_{rx} = -\mu\left[\frac{\partial v}{\partial r} + \frac{\partial v}{\partial x}\right],$$
$$\tau_{xx} = -2\mu \frac{\partial u}{\partial x}, \qquad \tau_{\theta\theta} = -2\mu \frac{v}{r} \tag{4}$$

Conservation of charge

$$\frac{\partial j_x}{\partial x} + \frac{1}{r}\frac{\partial}{\partial r}(rj_r) = 0 \tag{5}$$

Equation (5) can be recast into a Laplace equation by using an electric potential ϕ which is defined as $\mathbf{j} = -\sigma\nabla\phi$, where σ is the electrical conductivity. The electric potential definition is used in this study.

Conservation of energy

$$\rho u\frac{\partial h}{\partial x} + \rho v\frac{\partial h}{\partial r} = \frac{\partial}{\partial x}\left(\frac{k}{C_p}\frac{\partial h}{\partial x}\right) + \frac{1}{r}\frac{\partial}{\partial r}\left(\frac{k}{C_p}r\frac{\partial h}{\partial r}\right) - S_R + \frac{j_x^2 + j_r^2}{\sigma}$$
$$+ \frac{5}{2}\frac{k_B}{e}\left(\frac{j_x}{C_p}\frac{\partial h}{\partial x} + \frac{j_r}{C_p}\frac{\partial h}{\partial r}\right) \tag{6}$$

where h, k, C_p, S_R, k_B, and e are the specific enthalpy, the thermal conductivity, the specific heat at constant pressure, the optically thin radiation loss, the Boltzmann constant, and the elementary charge, respectively. The energy exchanges due to spatial variation of the pressure are neglected.

Since rotational symmetry was postulated, only B_θ is required for the momentum equations, which can be obtained by the expression

$$B_\theta = \frac{\mu_0}{r}\int_0^r j_x \xi \, d\xi \tag{7}$$

where μ_0 is the magnetic permeability of vacuum.

2.4. Boundary Conditions

At the wall, a constant temperature (at 1000 K based on Ref. 11) boundary condition and no slip boundary condition for the velocity fields are used in this study. High electrical conductivity with a floating current condition

for the electric field are imposed at the bottom anodic wall surface. For the centerline ($r=0$), the symmetry boundary condition with zero normal velocity component is specified. Since no interface deformation between the molten pool and plasma phase is considered in this study, the normal velocity at the interface is set to zero with shear stress continuity across the interface. It should be mentioned that the usual boundary condition for the tangential velocity at the interface in a welding problem considers the surface tension driving force (Marangoni force) only. However, the surface tension is a complicated function of material composition, and information about the thermal behavior of the surface tension for the present problem is not available. Moreover, for the free-burning arc problem, the Lorentz force-induced convective flow is much stronger and tends to overcome the surface-tension-induced force.[9] Thus, the Marangoni effect is not considered in this study. The heat flux continuity at the interface is used for the energy conservation. No shielding gas is used in this study. The above-mentioned boundary conditions can be translated into mathematical expressions as follows:

At the wall:

$$u_p = v_p = u_m = v_m = 0 \tag{8a}$$

$$T = 1000 \text{ K} \tag{8b}$$

$$\left.\frac{\partial \phi}{\partial r}\right|_{r=R} = 0, \qquad \left.\frac{\partial^2 \phi}{\partial x^2}\right|_{x=0} = 0 \tag{8c}$$

At the interface ($x=3.55$ cm):

$$u_p = u_m = 0 \tag{9a}$$

$$-\mu_p\left[\frac{\partial v_p}{\partial x}+\frac{\partial u_p}{\partial r}\right] = -\mu_m\left[\frac{\partial v_m}{\partial x}+\frac{\partial u_m}{\partial r}\right] \tag{9b}$$

$$-\kappa_p \frac{\partial T_p}{\partial x} = 1\kappa_m \frac{\partial T_m}{\partial x} \tag{9c}$$

$$-\sigma_p \frac{\partial \phi_p}{\partial x} = -\sigma_m \frac{\partial \phi_m}{\partial x} \tag{9d}$$

At the centerline:

$$\frac{\partial u_p}{\partial r} = \frac{\partial u_m}{\partial r} = \frac{\partial T_p}{\partial r} = \frac{\partial T_m}{\partial r} = \frac{\partial \phi}{\partial r} = v_p = v_m = 0 \tag{10}$$

At the top of the reactor (open boundary):

$$\frac{\partial u_p}{\partial x}=\frac{\partial u_m}{\partial x}=\frac{\partial T_p}{\partial x}=\frac{\partial T_m}{\partial x}=v_p=v_m=0, \qquad \phi=V_{\text{drop}} \tag{11}$$

where V_{drop} is the voltage specified by the input power. At the cathode tip, the current boundary condition is imposed, which represents cathode emission of electrons. The current is specified at 1 mm below the cathode with an exponential function as

$$j_x=j_{x_{\max}}\exp(-r/r_0) \tag{12}$$

where $j_{x_{\max}}$ is the maximum current at the cathode tip and r_0 is the cathode spot radius. Both $j_{x_{\max}}$ and r_0 vary with the operating condition and the cathode shape and can be determined from experimental observation.[11]

3. MATHEMATICAL MODEL OF USBM ARC MELTER

3.1. Geometric Configuration

The USBM plasma arc melter system is composed of a continuous feed system, the three-phase electric arc melting furnace, an off-gas control system, and utilities.[1] The arc furnace is cylindrical in shape, approximately 2 m high and 1.3 m wide. Figure 2 shows the melter configuration and the created model configuration. Unmelted soil is introduced into the melter 0.5 m above the melt surface and feeds into the melted pool. The melted

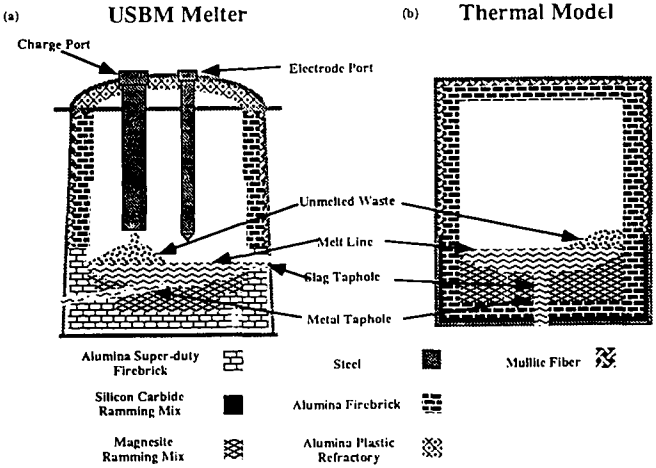

Fig. 2. (a) Geometry of the USBM arc melter. (b) Simplified USBM arc melter geometry for thermal model considered in this study.

soil then travels out the bottom of the melter. The furnace can process as high as 680 kg/h of contaminated soil with a power input rate of up to 800 kW.[1] The main focus of this study is on the electric arc melting furnace, where the thermal treatment of the contaminated soil takes place. The interaction of the plasma and the molten pool is studied by considering the flow and heat addition due to joule heating.

3.2. Assumptions

A steady, axisymmetric, and laminar flow is assumed. Heat is transferred by diffusion, advection, and gray-body radiation. Radiation is considered only from surface to surface through the air. The model is taken as two-dimensional axisymmetric. Momentum equations are solved only in the molten soil. Electric field calculations are not included; rather, the heat input into the melted soil is by a constant source term.

3.3. Governing Equations

Based on the above assumptions, the governing equations may be written in terms of cylindrical coordinates (r, x, θ). The conservation of mass is the same as Eq. (1), while the conservation of momentum equations are the same as Eqs. (2)–(4) without the electromagnetic field forces.

Conservation of energy

$$\rho C_p\left(u\frac{\partial T}{\partial x}+v\frac{\partial T}{\partial r}\right)=\frac{\partial}{\partial x}\left(k(T)\frac{\partial T}{\partial x}\right)+\frac{1}{r}\frac{\partial}{\partial r}\left(k(T)r\frac{\partial T}{\partial r}\right)+Q(x,r) \qquad (13)$$

where T is temperature and $Q(x, r)$ is the volumetric heat source varying with position.

3.4. Boundary Conditions

The outside surface of the furnace has a convective heat transfer coefficient of 100 W/m-K with a convective temperature of 300 K. Where the unmelted soil is introduced into the melter, a temperature boundary condition of 300 K is applied. Velocity boundary conditions are no slip condition between the molten soil and the solid bricks that the soil comes in contact with. The radial velocity along the centerline is also specified as zero.

4. NUMERICAL METHOD

The governing equations in Section 2 are solved by using the SIMPLEC algorithm.[12] The energy and the electron conservation equations are solved

by using the same procedure described by Patankar.[13] In order to treat the solid/liquid boundary in the molten pool, the momentum equations need special treatment. The velocity inside the control volume which contains the two-phase interface are set to zero. This approach has been used by Basu and Date,[14] and briefly described in the following. Instead of the latent heat content of a control volume used by Basu and Date,[14] the soil mixture temperature defined as the following is used to identify the liquid control volume:

$$\begin{aligned} T &= \frac{h_m}{C_{pm} + T_0} && \text{for } T < T_{\text{melt}} \\ T &= \frac{(h_m - L_m)}{C_{pm}} + T_0 && \text{for } T \geq T_{\text{melt}} \end{aligned} \tag{14}$$

The velocity of any control volume with $T < T_{\text{melt}}$ is set to zero. After the liquid control volumes are identified, the pressure correction boundary condition is applied. Following the notation used in Ref. 13, the pressure correction boundary conditions at the solid/liquid interface can be written as follows:

$$\begin{aligned} &\text{If } T_P \geq T_{\text{melt}} \text{ and } T_E < T_{\text{melt}};\ d_E^P = 0 \\ &\text{If } T_P \geq T_{\text{melt}} \text{ and } T_W < T_{\text{melt}};\ d_W^P = 0 \\ &\text{If } T_P \geq T_{\text{melt}} \text{ and } T_N < T_{\text{melt}};\ d_N^P = 0 \\ &\text{If } T_P \geq T_{\text{melt}} \text{ and } T_S < T_{\text{melt}};\ d_S^P = 0 \end{aligned} \tag{15}$$

Details of the code validation tests are given in Ref. 7.

For the simulation of the full-scale USBM arc melter, a commercially available finite-element code FIDAP[15] is used.

5. RESULTS AND DISCUSSIONS

Before we discuss the calculated results, the air plasma properties are compared with those of argon. Figure 3 shows the temperature dependence of thermodynamic and transport properties of air and argon. Heat capacity at constant pressure, density, thermal conductivity, electrical conductivity, molecular viscosity, and radiation heat loss are shown. These properties are taken from Ref. 16. Since the air is treated as a mixture of diatomic gases, the thermodynamic and transport properties show two peaks on the temperature ranges considered in this study. The first peak, around 7000 K in heat capacity and thermal conductivity, is due to the dissociation of the nitrogen gas, and the second peak is due to the ionization of the nitrogen. One of the unique differences between air and argon is that the air properties show two peaks while the argon has only one peak in the temperature ranges we

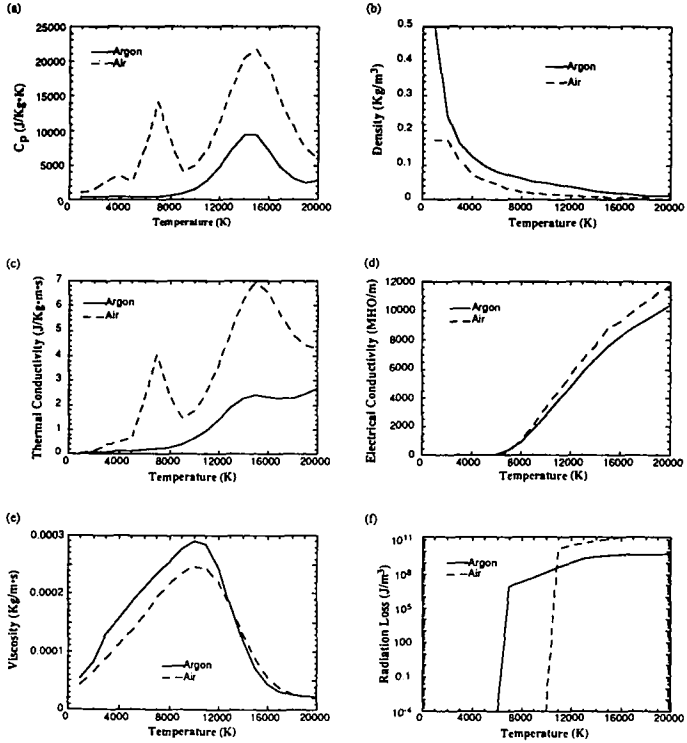

Fig. 3. Plasma thermodynamic and transport properties used in this study: (a) heat capacity; (b) density; (c) thermal conductivity; (d) electrical conductivity; (e) viscosity; (f) radiation loss.

considered. This is because the argon is a monatomic gas. The peak occurring in argon properties is due to the ionization of the argon at that temperature. It should be noted here that air has substantially higher heat capacity, thermal conductivity, and radiation energy loss than the argon at the same temperature. The density and the viscosity of the soil are taken from Buelt *et al.*[17] The other thermophysical properties of the soil used for this study are from Henderson and Taylor.[18] In the solid domain, the viscosity is set to 10^{16} kg/m-s in order to ensure that no flow is allowed.

Two different cases are simulated with different gaps between the cathode and the molten surface. Figure 4 shows the comparisons of the temperature fields of the argon and air plasmas over the molten soil field. In the case of air plasma, the plasma volume is smaller than that of argon plasma at the same input power (5 kW input power is used for both argon and air cases). There are three factors for this small plasma volume for air.

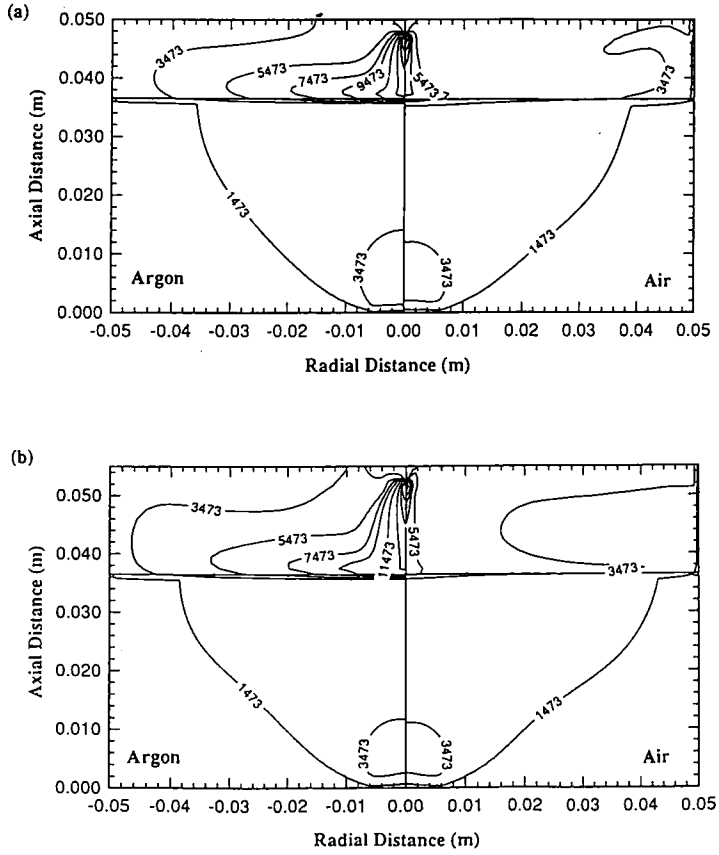

Fig. 4. Isotherms inside the plasma arc melter (from 1473 to 18473 K with 2000 K increment) for a current density of 200 A and 5 kW input power. Results on the left-hand side are the argon plasma case and those on the right-hand side are the air plasma case (a) for the 1 cm arc length case (gap = 1 cm), and (b) for the 1.5 cm arc length case (gap = 1.5 cm).

One is significant radiation energy loss of air plasma at the high temperatures (see Fig. 3f). This is one reason that the air plasma has low energy efficiencies as described below (see Table I). The second factor is that the heat capacity of the air is an order higher than that of argon (see Fig. 3a) so that more energy is absorbed by the air at the same temperature. The third is that the thermal conductivity of the air plasma is higher than that of argon (see Fig. 3c). Owing to the high thermal conductivity of the air, heat conduction plays an important part on heating the soil surface. The melt front in the soil region shows a bowl shape with maximum temperature occurring at the bottom of the reactor because of the high current density collected at the

Table I. Percentage of the Power Absorbed by the Melt Pool to the Total Power for Different Operating Conditions

	Gap = 1 cm		Gap = 1.5 cm	
Total power (kW)	Argon $I = 200$ A	Air $I = 200$ A	Argon $I = 200$ A	Air $I = 200$ A
5	38.3 (28.50)[a]	36.2 (30.13)	40.2 (31.03)	38.8 (32.75)
7.5	27.5 (28.82)	27.2 (31.45)	26.0 (27.69)	37.1 (33.96)

[a]The number in parentheses is the percent ratio of the melt volume to the total soil volume.

bottom. In Fig. 4, the maximum temperature near the bottom of the reactor increases as the arc length becomes shorter. Soil heating efficiency is calculated for different arc operating conditions and listed in Table I. The efficiency is defined as the ratio between the power absorbed by the melt pool to the total power of the reactor. The melted soil volume percentage to the total soil volume is also listed in Table I. It was found that increasing the voltage for the same current does not affect the melt volume significantly[7] and thus no attempts were made to reveal the effects of different voltages of the plasma. By comparing the energy absorbed in the soil, the argon plasma cases show better energy efficiency than that of air at the same operating conditions. However, the fraction of the melted volume to the total soil volume shows that the air plasma case has more molten soil than that of argon. This can be explained by the fact that in the case of the argon plasma the joule heating is concentrated near the center of the molten pool which locally heats the soil near the center of the reactor. In the case of the air plasma, the current arriving at the molten surface is more radially spread, which results in more uniform heating of the soil. In order to show this effect, interfacial temperatures and currents are shown in Fig. 5. For the air plasma case, the interface shows higher temperatures than that of argon toward the wall. The difference between the temperatures becomes significant

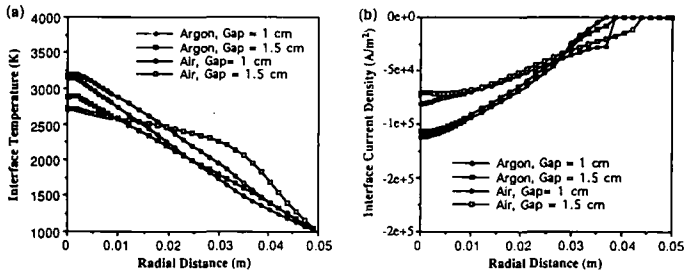

Fig. 5. (a) Plasma-soil interfacial temperature profile. (b) Plasma-soil interfacial normal current profile.

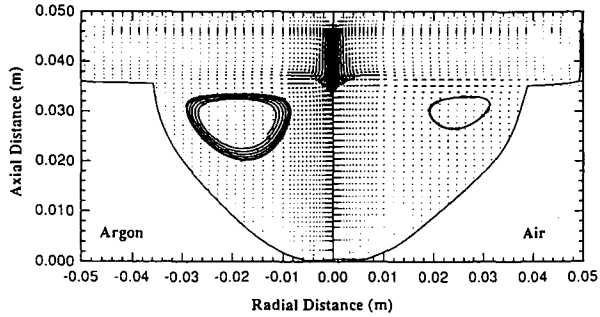

Fig. 6. Velocity vector inside the plasma arc melter for a current density of 1 cm gap, 200 A, and 5 kW input power. The loops inside the melt represent streaklines. Results on the left-hand side are for the argon plasma case and those on the right-hand side are for the air plasma case.

as the arc length increases. For the short arc, the temperature at the interface is higher than for the long arc, as one can expect. The maximum currents at the interface for the short arc are higher than those of the long arc. For the longer arc, slightly higher currents than those of the short arc can be found far from the arc core since the electrical conductivity of the plasma and the melt pool is relatively evenly distributed over the interface.

Figure 6 shows that the induced flow fields in the molten soil region have strong clockwise convection occurring on the right-hand side of the reactor. This convection is a result of the combined effects of the shear and buoyancy induced force.[7] For the air plasma case, the center of the circulation is far from the centerline compared to the argon plasma case. As shown in Figs. 4 and 5, the steep temperature gradient occurs near the center of the reactor for the argon plasma. Thus, the magnitude of the buoyancy force is higher near the center for the argon plasma case while the recirculation occurs far from the centerline in the air plasma case. Because of the large density difference caused by the temperature gradient inside the molten soil, the induced natural convection force contributes to the clockwise convection in the melt pool.[7]

Results from the plasma arc simulations in this paper show that approximately 38% of the heat goes into the soil for the 1-cm gap case, while the rest is radiated to the outer vessel walls and convected out through the off-gas system. Therefore, this simulation is with 38% of the total power input. The results of the USBM melter are shown in Fig. 7 and 8. Figure 7 is the finite-element mesh created for the model. Figure 8 shows the temperature contours for 38% of the power entering the soil. The power is directed into a small region directly below the electrodes. The heat generation rate

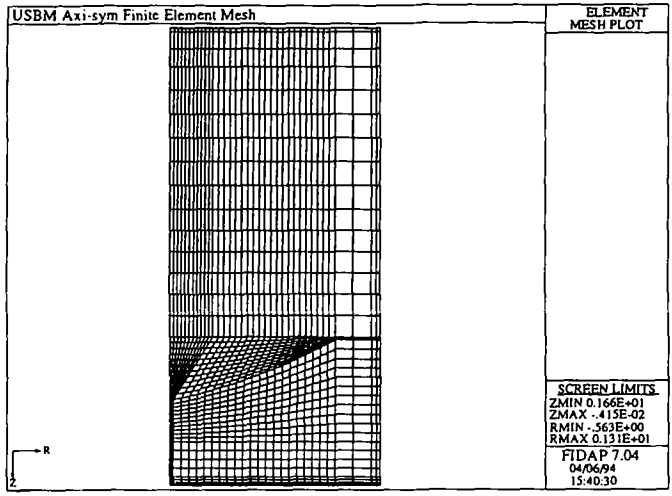

Fig. 7. Finite-element mesh of USBM melter facility used in this study.

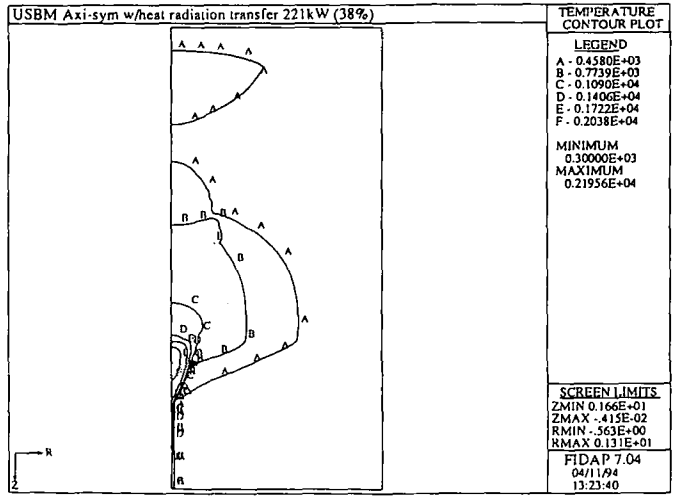

Fig. 8. Temperature contours of radiation/conduction model for USBM melter facility.

in the soil is 38 MW/m^3. The maximum temperature in the soil is 2195 K and occurs at the center of the region where heat is generated. The exit temperature of the molten soil is 1600 K. These temperatures agree well with experimental results.[19]

6. CONCLUSIONS

The following conclusions are made in this study:

1. At the same input power, the volume of air plasma is significantly less than that of argon plasma because of the high heat capacity, radiation loss, and thermal conductivity of the air.
2. The maximum temperature inside the melt pool is higher in an argon plasma arc melter than that in an air plasma owing to the concentrated currents arriving at the melt pool surface.
3. Total melted volume of the air plasma arc melter is larger than that of the argon plasma since the heat is dissipated more uniformly inside the melt pool for the air plasma.
4. Heat transfer calculations have been performed for the USBM melter facility. Included in the calculation is surface-to-surface, gray-body radiation, conduction, and advection within the molten soil. Results show a maximum temperature of 2195 K at the center of the heat generation, and a molten soil exit temperature of 1600 K.

ACKNOWLEDGMENT

The authors thank Mr. E. B. Nielson for providing the figures. Valuable comments from Dr. M. Mckellar are gratefully acknowledged. This work was performed under the auspices of the U.S. Department of Energy, contract DE-AC07-76-ID01570, and was supported in part by the Buried Waste Integrated Demonstration Program.

REFERENCES

1. L. L. Oden, W. K. O'Connor, P. C. Turner, N. R. Soelberg, and G. L. Anderson, Baseline Tests for Arc Melter Vitrification of INEL Buried Wastes, Volume 1: Facility Description and Summary Data Report, EGG-WTD-10981, November 19, 1993.
2. K. C. Hsu and E. Pfender, *J. Appl. Phys.* **54**, 3818 (1983).
3. M. C. Tsai and S. Kou, *Int. J. Heat Mass Transfer* **33**, 2089 (1990).
4. E. Pfender, *Pure Appl. Chem.* **52**, 1773 (1980).
5. J. J. Gonzalez, A. Gleizes, P. Proulx, and M. Boulos, *J. Appl. Phys.* **74**, 3065 (1993).
6. K. Taniuchi, *High Temp. Mater. Process.* **11**, 369 (1993).
7. S. Paik and H. D. Nguyen, "Numerical modeling of multiphase plasma soil flow and heat transfer in an electric arc furnace," to appear in *Int. J. Heat Mass Transfer.*
8. P. C. Kong, J. D. Grandy, A. D. Watkins, T. L. Eddy, and G. L. Anderson, Bench-Scale Arc Melter for R&D in Thermal Treatment of Mixed Wastes, EGG-MS-10646, Idaho National Engineering Laboratory (INEL), Idaho Falls, Idaho, May 1993.
9. L. Gu, R. Jensen, A. E. Arntsberg, and J. A. Bakken, Study on Silicon Vapor Contaminated Argon Arcs and the Metal Pools, 11th International Symposium on Plasma Chemistry **1**, 222, Loughborough, England, Aug. 22–Aug. 27, 1993.

10. R. B. Bird, W. E. Stewart, and E. N. Lightfoot, *Transport Phenomena*, Wiley, New York (1960).
11. K. C. Hsu, "A self-consistent model for the high-intensity free-burning argon arc," Ph.D Thesis, Dept. of Mech. Eng., Univ. of Minnesota, 1982.
12. J. P. Vandoormal and G. D. Raithby, *Numer. Heat Transfer* **7**, 147 (1984).
13. S. V. Patankar, *Numerical Heat Transfer and Fluid Flow*, 1st edn., Hemisphere, New York (1980).
14. B. Basu and A. W. Date, *Int. J. Heat Mass Transfer* **33**, 1149 (1990).
15. M. S. Engelman, FIDAP Manual, Version 7.0, Fluid Dynamics International, Evanston, Illinois (1993).
16. Seungho Paik, Y. P. Chyou, and E. Pfender, "Thermodynamic and transport properties: Ar, H_2, N_2, O_2, Air, CO, CO_2, H_2O, H_2/HCl," under ALCOA Contract, Dept. of Mech. Eng., Univ. of Minnesota, 1987.
17. J. L. Buelt, V. F. FitzPatrick, C. L. Timmerman, J. G. Carter, and K. H. Oma, *In Situ* Vitrification of Transuranic Waste: An Updated Systems Evaluation and Applications Assessment, PNL-4800 suppl-1, US-70, March 1987.
18. J. B. Henderson and R. E. Taylor, Thermophysical Properties Research Laboratory, TPRL-1238, School of Mech. Eng., Purdue University, West Lafayette, Indiana, February (1993).
19. G. Anderson, private communication, April 1994.